Journal of Biomedical Optics

BiomedicalOptics.SPIEDigitalLibrary.org

In vivo photoacoustic microscopy of human cuticle microvasculature with single-cell resolution

Hsun-Chia Hsu
Lidai Wang
Lihong V. Wang

SPIE.

Hsun-Chia Hsu, Lidai Wang, Lihong V. Wang, "*In vivo* photoacoustic microscopy of human cuticle microvasculature with single-cell resolution," *J. Biomed. Opt.* **21**(5), 056004 (2016), doi: 10.1117/1.JBO.21.5.056004.

In vivo photoacoustic microscopy of human cuticle microvasculature with single-cell resolution

Hsun-Chia Hsu, Lidai Wang,[†] and Lihong V. Wang[*]
Washington University in St. Louis, Department of Biomedical Engineering, Optical Imaging Laboratory, One Brookings Drive, St. Louis, Missouri 63130, United States

Abstract. As a window on the microcirculation, human cuticle capillaries provide rich information about the microvasculature, such as its morphology, density, dimensions, or even blood flow speed. Many imaging technologies have been employed to image human cuticle microvasculature. However, almost none of these techniques can noninvasively observe the process of oxygen release from single red blood cells (RBCs), an observation which can be used to study healthy tissue functionalities or to diagnose, stage, or monitor diseases. For the first time, we adapted single-cell resolution photoacoustic (PA) microscopy (PA flowoxigraphy) to image cuticle capillaries and quantified multiple functional parameters. Our results show more oxygen release in the curved cuticle tip region than in other regions of a cuticle capillary loop, associated with a low of RBC flow speed in the tip region. Further analysis suggests that in addition to the RBC flow speed, other factors, such as the drop of the partial oxygen pressure in the tip region, drive RBCs to release more oxygen in the tip region. [DOI: 10.1117/1.JBO.21.5.056004]

Keywords: single-cell resolution photoacoustic microscopy; cuticle capillaries; oxygen saturation of blood; directional derivative of oxygen saturation of blood; speed of blood flow; total hemoglobin concentration; time derivative of oxygen saturation of blood.

Paper 150877R received Jan. 1, 2016; accepted for publication Apr. 19, 2016; published online May 18, 2016.

1 Introduction

The microcirculation comprises microvascular networks of arterioles, capillaries, and venules, which are fundamental for thermoregulation and for transporting nutrients and gases to maintain the metabolism of cells.[1] However, under disease states, such as severe hemorrhage, cardiogenic shock, sepsis,[1,2] and systemic scleroderma,[3–5] the associated dysfunction of the microcirculation may cause heterogeneous hypoxia, impairing cell functioning in tissues and even causing multiple organ failures.[1,2] In other cases, hypertension and diabetes mellitus can cause microvascular complications, such as microvessel rarefaction and retinopathy, respectively.[6,7] Tumors will often induce angiogenesis of the microvascular system in their microenvironment.[8] To better understand the fundamental mechanisms of these diseases, diagnose them in early stages, and evaluate the effectiveness of various therapies, it is essential to develop tools to monitor important microvascular parameters of blood perfusion. These parameters include function capillary density (which is defined as the total length of capillaries perfused by RBCs per observed area in units of cm^{-1}),[1] total hemoglobin concentration (C_{Hb}), the oxygen saturation of blood (sO_2), the directional derivative of sO_2 along the blood flow direction (DsO_2), and the speed of blood flow (v_{Hb}).[9]

Primary medical imaging modalities, such as single-photon emission computed tomography, functional magnetic resonant imaging, positron emission tomography, ultrasonography, and diffuse optical tomography, have been used for years to image cardiovascular or cerebral blood flow.[10–14] Additionally, contrast-enhanced ultrasonography, which detects nonlinear oscillation of microbubbles (only a few microns in size) under low mechanical index conditions, has been applied to imaging blood perfusion around focal liver lesions and the renal cortex.[15–17] Even though these techniques are the best we have to date to image blood flows in organs deep in the body, they are limited by their millimeter-size resolution. Thus, these modalities are not efficient in monitoring microcirculation, which in general contains vessels smaller than 100 μm.[1]

As an alternative, the cutaneous and sublingual microcirculations have been proposed as a representative model for visceral microcirculation, because they are accessible by optical-based imaging techniques, which provide higher resolution than most other imaging modalities.[18–20] Patients with chronic diseases such as hypertension, renal disease, and coronary artery disease have been observed to have distinct cutaneous microvascular parameters.[6,21,22] Monitoring cutaneous microvascular functioning provides valuable information for evaluating peripheral microvascular diseases, such as Raynaud's disease and peripheral arterial disease.[4,23,24] To this end, optical scattering-based techniques such as laser Doppler imaging,[22,25] near-infrared spectroscopy,[26,27] and reflectance spectroscopy[28,29] are used to detect scattered light from tissues. Over a submillimeter sampling volume, laser Doppler imaging can measure the average speed of flow, and near-infrared spectroscopy and reflectance spectroscopy can measure both the average flow speed and the oxygen saturation. On the wide-field scale, nailfold videomicroscopy,[4,30,31] orthogonal polarization spectral imaging,[32,33] sidestream dark field imaging,[34] and optical coherent tomography[35,36] can provide wide-field information about function capillary density and the speed of flow, with lateral resolutions ranging from submicrons to around 15 μm, which covers from the thinnest capillaries to the wider arterioles and venules. The imaging depth can go as deep as 400 μm for nailfold videomicroscopy and around 1 to 3 mm for optical-based techniques. Combined with an endoscope, these

*Address all correspondence to: Lihong V. Wang, E-mail: LV.Wang@outlook.com

[†]Present address: City University of Hong Kong, Department of Mechanical and Biomedical Engineering, Tat Chee Avenue, Kowloon, Hong Kong, China.

1083-3668/2016/$25.00 © 2016 SPIE

modalities can image the gastric or intestinal microcirculation with a tolerable compromise of image quality. However, none of these imaging modalities can provide sO_2 and v_{Hb} information at the same time.

In recent years, optical resolution photoacoustic microscopy (OR-PAM) has shown promise in *in vivo* microvascular imaging, with its ability to provide wide-field, capillary-resolving, and hemoglobin-sensitive images.[37–43] Combined with the flow speed imaging techniques reported previously,[44–46] OR-PAM has been demonstrated as a powerful tool to acquire such important parameters of the microcirculation as sO_2, DsO_2, C_{Hb}, v_{Hb}, and the metabolic rate of oxygen in tissues.[47,48] In this study, we implemented dual-wavelength *in vivo* OR-PAM for investigating oxygen release in cuticle capillaries. This is the first time that oxygen release dynamics in human cuticle capillaries have been monitored. The correlation between oxygen release and the speed of RBCs and between oxygen release and the first-order time-derivative of sO_2 have also been analyzed in a cuticle capillary. The spatial- and time-resolved information acquired by OR-PAM may help in early-stage diagnosis of perivascular diseases, such as Raynaud's syndrome, and in diagnosing heterogeneous microcirculation of interior organs.

2 Methods

2.1 *Experimental Protocol*

Nine healthy, consenting volunteers (with ages ranging from 23 to 30; seven males and two females) were recruited in this study. For each volunteer, we imaged the cuticle capillaries in the fourth finger (the ring finger) of the left hand.[36] Before each experiment, the volunteer rested in the temperature-controlled laboratory (at 20°C) for 15 min to adapt to the environmental temperature, since nailfold microcirculation is known to be sensitive to the surrounding temperature. The imaged area was then cleaned with alcohol swabs, and the hand was comfortably put on a homemade hand mount, without occlusion of blood flow, as shown in Fig. 1. During the data acquisition period, the photoacoustic (PA) scanning head was scanned over a single cuticle capillary at a time for three-dimensional imaging, with a 10-Hz C-scan rate (high-speed scanning mode) for about 40 s. At least three cuticle capillaries were recorded for each volunteer. The total experimental time spent on a volunteer was <1.5 h, including rests every 20 min to prevent numbness of the extremities. The human study was approved by the Institutional Review Board of Washington University in St. Louis, and the pulse energies of the excitation lasers used in each experiment were within the American National Standards Institute (ANSI) laser safety limit (20 mJ · cm^{-2}).

2.2 *System Setup*

In order to monitor the real-time microcirculation of a single cuticle, dual-wavelength excitation at 532 nm (SPOT, Elforlight, Northants, United Kingdom) and 559 nm (INNOSLAB, Edgewave, Würselen, Germany) was implemented on a high-speed voice-coil scanning PA microscope,[49] shown in Fig. 1. The two short-pulse (<10 ns) excitation beams, with a 10-μs

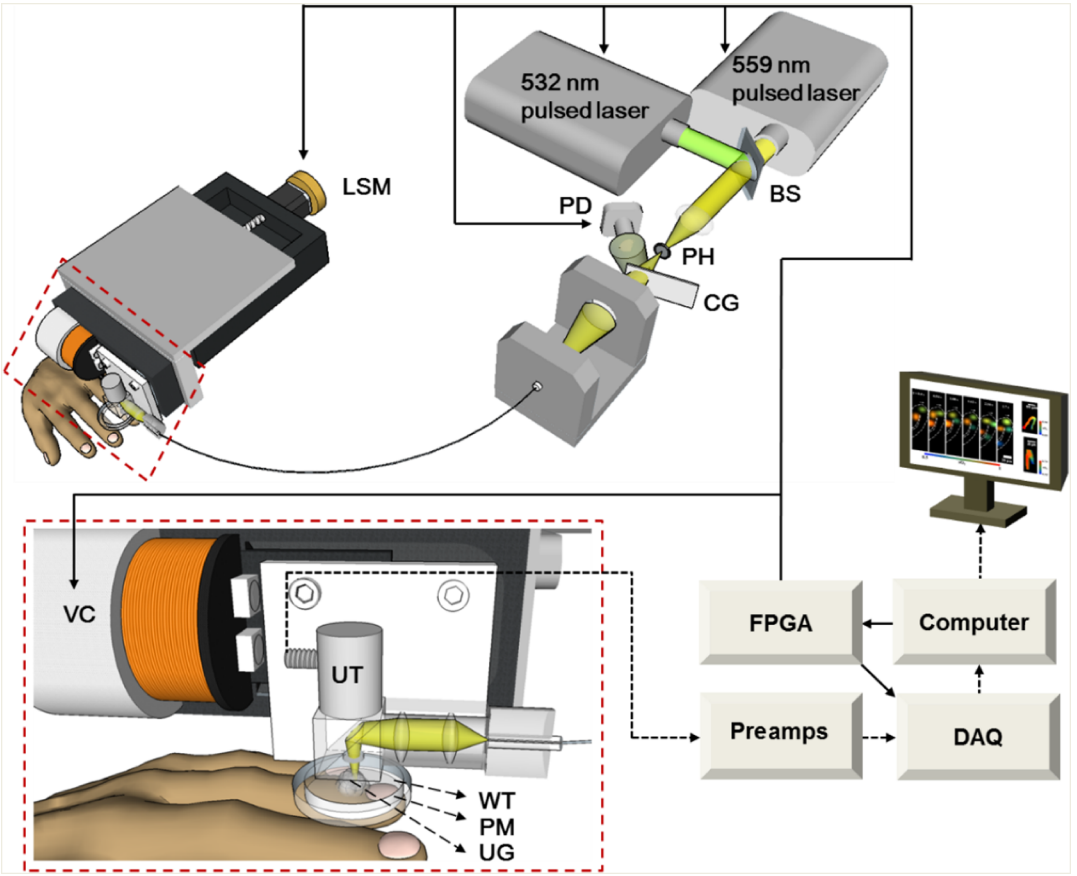

Fig. 1 Schematic of the single-cell OR-PAM system. BS, beam splitter; CG, coverglass; LSM, linear step motor; PD, photodiode; PH, pin hole; PM, plastic membrane; UG, ultrasound gel; UT, ultrasound transducer; VC, voice coil motor; and WT, water.

temporal delay between them, were first attenuated, combined, and passed through an optical spatial filter made of a spherical lens and a pinhole (50 μm in diameter; P50C, Thorlabs, Newton, New Jersey); then they were guided into a customized photonic crystal fiber (Thorlabs, Newton, New Jersey). The other end of the fiber was connected to the scanning PA probe. The output beams from the fiber were focused by a lens pair with a numerical aperture of 0.1 in water and were reflected by an acoustic-optical beam combiner made of two right-angle prisms sandwiching a coated aluminum layer on the hypotenuse faces. The emitted PA signals in the reflection direction were collected by an acoustic lens and then detected by a 50-MHz ultrasonic transducer (V214, Olympus NDT, Pennsylvania). The received PA signals were amplified (ZFL-500LN+, Mini-circuits, New York), filtered, and then digitized by a data acquisition (DAQ) system (ATS9350, Alazar Tech. Inc., Quebec, Canada). The optical focusing and the bandwidth of the transducer provided 3-μm lateral resolution and 15-μm axial resolution, respectively. In order to compensate for variations of the optical energy, pulse by pulse, a photodiode was set up after the optical spatial filter. The laser pulse energy on the sample surface was between 35 and 50 nJ in high-speed mode with the laser repetition rate of 20 kHz.

During single cuticle capillary imaging, the PA probe mounted on the voice-coil motor was driven to scan linearly with 100 Hz (B-scan) frequency within a 250-μm range. Combined with an additional linear translational stage (PLS-85, PI miCos, Eschbach, Germany), the system was set to repeatedly acquire 250 μm $\times$ 40 μm C-scan images at 10 Hz. The lasers, photodiode, and DAQ system were synchronously triggered at 20 kHz by a programmed field-programmable gate array card (PCI-7830R, National Instruments, Austin, Texas). This dual-wavelength high-speed PA microscopy has been previously demonstrated for measuring sO_2 and blood flow speed in mouse capillaries.[49]

2.3 *Principle of Oxygen Saturation of Blood Measurement*

After C-scan, images have been acquired with two wavelengths, and the sO_2 values can be calculated pixel-by-pixel according to the method in Refs. 50, 51. In short, the PA amplitude P at the i'th wavelength λ_i from a single pixel is related to the molar extinction coefficients of deoxy- and oxy-hemoglobin $[\varepsilon_{\mathrm{HbR}} \times (\lambda_i), \varepsilon_{(\mathrm{HbO_2})} \times (\lambda_i)]$, the concentrations of deoxy- and oxy-hemoglobin $\{[\mathrm{HbR}], [\mathrm{HbO_2}]\}$, and the optical fluence F as follows:

$$P(\lambda_i) \sim \{\varepsilon_{\mathrm{HbR}}(\lambda_i)[\mathrm{HbR}] + \varepsilon_{\mathrm{HbO_2}}(\lambda_i)[\mathrm{HbO_2}]\} \cdot \mathrm{F}(\lambda_i).$$

In order to solve for [HbR] and $[\mathrm{HbO_2}]$, two wavelengths are selected to build up two independent equations. To calibrate the sO_2 calculation, the optical properties of the tissue should be considered as well. We followed the same procedure as in Ref. 50 to calibrate the system. To mimic the optical properties of human tissue, the calibration was done in mouse experiments at a depth similar to that of the cuticle capillaries in human tissue.

3 Results

3.1 *Monitoring of Oxygen Saturation of Blood Dynamics in Cuticles*

Figures 2(a)–2(c) show a top view (C-scan) and a cross-sectional view (B-scan) of the typical morphology of finger cuticle

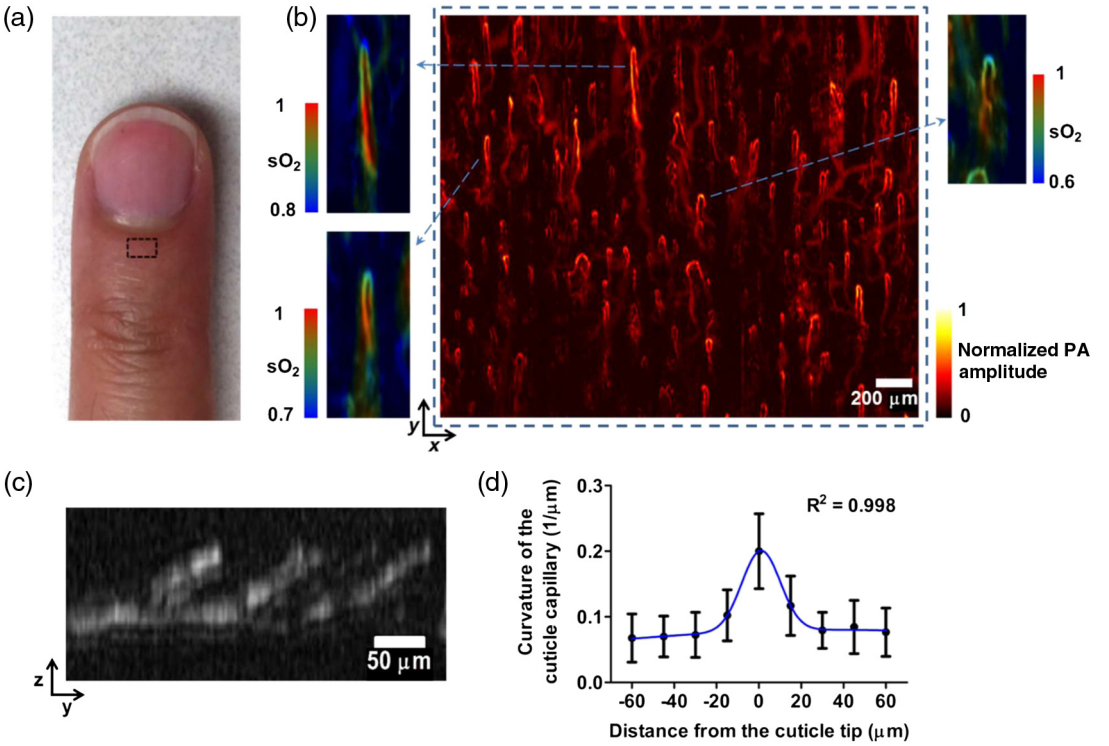

Fig. 2 (a) Photograph of a finger with the imaged area boxed. (b) Wide-field PA image of cuticle capillaries shown with normalized PA amplitude. The insets show sO_2 images of selected cuticles with different color bars. (c) B-scan image of cuticle capillary loops. (d) Curvature along the cuticles (fitting: sum of two Gaussians).

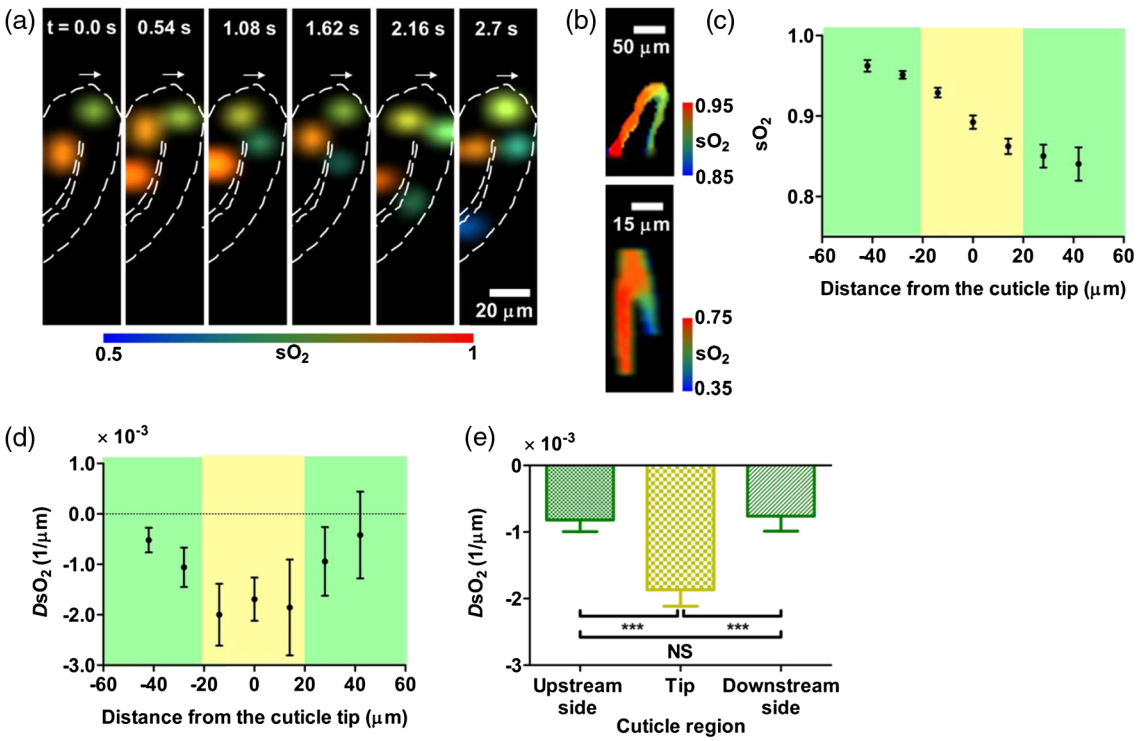

Fig. 3 (a) Selected time-lapse images of single-RBC sO_2 (Video 1, MPEG, 207 KB) [URL: http://dx.doi.org/10.1117/1.JBO.21.5.056004.1]. (b) Time-averaged images (~10 s) of all time-lapse frames of sO_2 imaging. (c) Time-averaged sO_2 along the length of a cuticle capillary loop (i.e., a trace of the blood flow). (d) Time-averaged directional derivative of sO_2 along the length of the loops. (e) Statistics of (d): paired Student's *t*-test between the tip region (yellow) and the two side regions (green). NS: not significant ($P = 0.48$), $^{***}P < 0.001$, and $n = 21$.

capillary loops. The acquisition time of a C-scan image was 75 s. The cuticle capillary loops angle toward the distal nail bed and gradually toward the epidermis. Figure 2(d) shows the result of using the curvature calculated from the C-scan images to quantitatively describe the geometric profile at different positions along the cuticles. The full width at half maximum distance is around 40 μm, which suggests that it is reasonable to define a region ± 20 μm from the position with maximal curvature as the tip region of a cuticle. It is also noticeable but not surprising to observe that in most cases the tip positions (0 μm) coincide with the uppermost ends of the cuticles in the B-scan images. In Fig. 2(b), the insets also show pixel-by-pixel calculation of sO_2 distribution in different areas of the cuticle capillary network with different color bars. The sO_2 reduction across the tip of a cuticle capillary is within 0.2. In high-speed scanning mode, the flow and the sO_2 of single RBCs can be resolved, as shown in the snapshots in Fig. 3(a) and Video 1. Figure 3(b) shows the results of time-averaging over all the frames of the sO_2 image. Around the cuticle tip (the most curved position along the cuticle), an abrupt drop in sO_2 can be observed. Figure 3(c) shows sO_2 versus s, where s denotes the displacement along the central axis of a cuticle capillary loop (i.e., the trace of the blood flow). The origin of s is coincident with the cuticle loop tip, and the RBCs flow from the negative coordinates (the upstream side of a cuticle vessel) to the positive coordinates (the downstream side). The sO_2 change with distance can be revealed more clearly by plotting the derivative of sO_2 with respect to s, which is defined as $DsO_2 \equiv \partial(sO_2)/\partial s$, as shown in Fig. 3(d). The DsO_2 values within ~15 μm the cuticle loop tips are approximately twice as high as those in regions 25 to

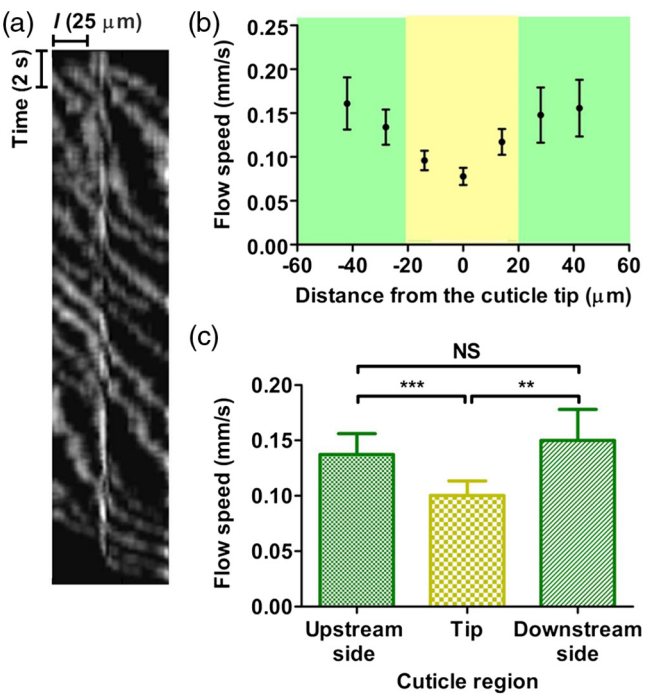

Fig. 4 (a) Image for speed measurement. (b) Time-averaged RBC flow speeds along the length of a cuticle loop. (c) Statistics of (b): paired Student's *t*-test between the tip region (yellow) and the two side regions (green). NS: not significant ($P = 0.45$), $^{***}P < 0.001$, $^{**}P < 0.01$, and $n = 18$.

40 μm away from the tip. The paired Student's t-test between the tip region (yellow) and two sides (green) validates that the cuticle loop tips have significantly greater decreases in sO_2 than the sides do.

3.2 *Measurement of Red Blood Cell Flow Speed*

By mapping the length of a curved cuticle loop s into a straight line l, Fig. 4(a) shows the method we used to measure the speed of RBCs flowing in cuticle capillary loops.[45] Based on Fourier analysis of the frames of a specific segment of a capillary loop acquired at different times, the longitudinal flow speeds of different segments in a cuticle can be determined by $v_{\mathrm{Hb}} = (\Delta s/\Delta t) = (\Delta l/\Delta t) = (N_t/N_l)(\Delta F_t/\Delta F_l)$. Here, N_t and N_l are the sampled temporal and spatial lengths and F_t and F_l are the temporal and spatial frequencies. From Fig. 4(b), we can observe that the time-averaged RBC flow speed within the region of 15 μm around the cuticle tip is approximately one-third lower than that in the regions between 25 to 40 μm away from the cuticle tip. A paired Student's t-test between the tip and side regions shows a significantly lower RBC flow speed around the tip region.

3.3 *Measurement of Hemoglobin Flux in Red Blood Cell Flow and Time Derivative of Oxygen Saturation of Blood*

As well as imaging sO_2, we can also image the relative concentration of hemoglobin (C_{Hb}) by summing the calculated images for oxy- and deoxyhemoglobin. To calculate the time-averaged hemoglobin flux, we assume that the concentration and the speed are independent variables, which means that the time average of the product of the two variables is approximately equal to the product of the two time-averaged variables (in case the variances of C_{Hb} and v_{Hb} are small), so we have $\overline{\Phi_{\mathrm{Hb}}} \approx \overline{C_{\mathrm{Hb}}} \cdot v_{\mathrm{Hb}}$, where v_{Hb} is the time-averaged RBC flow speed around x. Figures 5(a) and 5(c) show a nearly flat

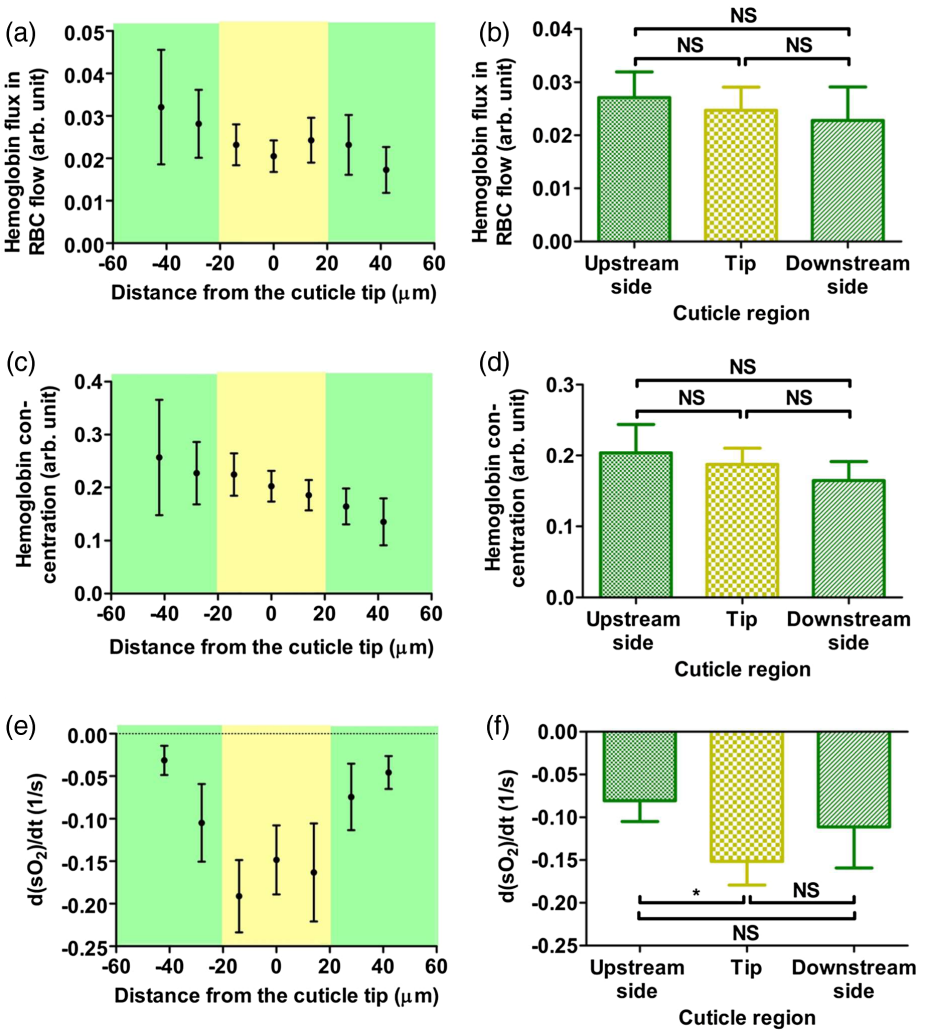

Fig. 5 (a) Time-averaged relative flow rates along the length of cuticle capillary loops. (b) Statistics of (a): paired Student's t-test between the tip region (yellow) and the two side regions (green). NS: not significant (up: $P = 0.24$, left: $P = 0.10$, right: $P = 0.40$), $n = 13$. (c) Time-averaging of hemoglobin concentration along the direction of the length of cuticles. (d) Statistics of (c): paired Student's t-test between the tip region (yellow) and the two side regions (green). NS: not significant (up: $P = 0.33$, left: $P = 0.45$, right: $P = 0.21$), $n = 18$. (e) Time-averaged values of $d(sO_2)/dt$ along the length of cuticle capillary loops. (f) Statistics of (e): paired Student's t-test between the tip region (yellow) and the two side regions (green). *$P = 0.03$, NS: not significant (up: $P = 0.07$, down: $P = 0.25$), $n = 15$.

trend, and the paired t-tests shown in Figs. 5(b) and 5(d) suggest that the hemoglobin flux in RBC flow is approximately the same along the cuticle capillary loops: the flow of RBCs is conserved. Under steady-state blood flow, $[d(\mathrm{sO}_2)/dt] = D\mathrm{sO}_2 \cdot (ds/dt)$. Similarly, we assume that both $D\mathrm{sO}_2$ and ds/dt are independent variables; we have $[d(\mathrm{sO}_2)/dt] \approx D\mathrm{sO}_2 \cdot v_{\mathrm{Hb}}$. The total time derivative of sO_2 along cuticle capillary loops is shown in Fig. 5(e). The p value between the upstream side and the tip is 0.03, and the p value between the downstream side and the tip is 0.07, according to the paired t-test shown in Fig. 5(f).

4 Discussion

In this study, we demonstrated the ability of single-cell resolution OR-PAM to monitor the microcirculation in cuticle capillaries with a temporal resolution of 0.1 s. Compared to nailfold video-capillaroscopy and optical computed tomography,[36] OR-PAM can not only image the morphology, dimensions, and vessel density of cuticle capillary loops, but also measure multiple hemodynamic parameters, such as sO_2, $D\mathrm{sO}_2$, C_{Hb}, and v_{Hb}. Monitoring these functional parameters at the fundamental level of the physiology of oxygen transport can potentially help biologists and physicians to understand the mechanisms of oxygen transport in the skin and to define clinical standards for early-stage diagnosis and evaluation of perivascular diseases, such as Raynaud's phenomenon and systemic scleroderma, before the capillaries undergo observable changes in morphology.

The time-averaged $D\mathrm{sO}_2$ results in Fig. 3(d) indicate that RBCs release more oxygen in the tip region over a length of around 30 μm then they do further down on the two sides. A similar result has been mentioned in one previous work, with no further investigation.[52] It is interesting to note that the 30-μm length is approximately equal to the length of a capillary loop in the dermal papillae in the skin outside of the cuticle area.[53] Capillary loops in dermal papillae are extensions of the subpapillary plexus in the reticular dermis, and they are responsible for oxygen and nutrient transport to living cells in the epidermis. Because nails are specialized structures of the skin,[54] cuticle capillaries and dermal capillaries should be functionally similar parts of the capillary loop system (except that cuticle capillaries extend toward the distal nail bed), it will not be surprising to discover that the tip region of a cuticle capillary releases more oxygen than the other regions.

In Figs. 4(b) and 4(c), the RBC flow speed is reduced in the tip region (around two-thirds of the speed in the side regions). In blood rheology, RBC flow in capillaries is treated as a non-Newtonian fluid because of the special viscoelasticity of erythrocytes, which complicates the RBC flow in a capillary.[55–57] The reduced RBC flow speed may result from deformation of RBCs and a consequent change of their viscoelasticity while passing through the highly curved pathway of the tip region. Another possibility is that RBCs partially accumulate in the tip region. In order to test this hypothesis, we examined the hemoglobin concentration and the hemoglobin flux along the cuticles. Further, we used a paired t-test to compare the effects of the straight part and the curved part of a cuticle on the hemoglobin flow and concentration. To improve the statistical accuracy, we excluded outlier data points that have large standard deviations (>30%). It can be seen that this hypothesis is not supported by the results in Figs. 5(a)–5(d), which show that both the flux of hemoglobin and the time-averaged hemoglobin concentration do not significantly differ between the side regions and the tip. Therefore, RBC flow is shown to be conserved along a cuticle capillary loop. The slower RBC flow in the tip region seems to meet a functional demand which requires a longer transit time of RBCs to release enough oxygen for metabolism. To investigate the relation between $D\mathrm{sO}_2$ and RBC flow speed, we calculated the time derivative of sO_2 along cuticle capillary loops. Without introducing physical cuffing and compression on the arm imaged, and without any extra physiological stimulation, we assumed that the RBC flow can be considered as in a steady or quasi-steady state, which means $[d(\mathrm{sO}_2)/dt] = D\mathrm{sO}_2 \cdot (ds/dt) + [\partial(\mathrm{sO}_2)/\partial t] \approx D\mathrm{sO}_2 \cdot (ds/dt)$.[58] Figures 5(e) and 5(f) show that RBCs release more oxygen per unit time in the tip region than in the sides. Although the statistics are not strongly significant ($p > 0.01$), this finding still suggests that there are factors other than RBC flow speed, such as partial oxygen pressure, that can drive RBCs to release more oxygen in the tip region.

In this investigation, our single-cell resolution OR-PAM system performed monitoring of several hemodynamic parameters on nine human volunteers. Cell-by-cell based statistics also provided insights. In the future, OR-PAM promises to help greatly in the early-stage diagnosis of perivascular diseases and to illuminate more fundamental mechanisms in hemodynamics.

5 Conclusion

In this paper, the cuticle microcirculations of healthy volunteers were monitored by real-time single-cell resolution OR-PAM. Hemodynamic parameters such as C_{Hb}, sO_2, $D\mathrm{sO}_2$, v_{Hb}, and relative blood flow rate were extracted from the images. A drop in $D\mathrm{sO}_2$ and slower RBC flow were observed in the tip region than in the side regions of a cuticle capillary loop. The conserved blood flow rate in a cuticle capillary loop and the drop in the time-derivative of sO_2 in the tip region suggest that the heterogeneity of the RBC flow speed over a cuticle capillary loop is not the only factor that determines the heterogeneity of the oxygen release in the loop.

Acknowledgments

This work was supported in part by the National Institutes of Health Grant Nos. DP1 EB016986 (NIH Director's Pioneer Award), R01 CA186567 (NIH Director's Transformative Research Award), and R01 CA159959. L. V. Wang has a financial interest in Microphotoacoustics, Inc., which, however, did not support this work. The authors want to specially thank Chenghung Yeh for suggestions on image processing, and all the volunteers who participated in this study.

References

1. D. De Backer et al., "Monitoring the microcirculation in the critically ill patient: current methods and future approaches," *Intensive Care Med.* **36**(11), 1813–1825 (2010).
2. D. De Backer, K. Donadello, and D. O. Cortes, "Monitoring the microcirculation," *J. Clin. Monit. Comput.* **26**(5), 361–366 (2012).
3. E. Carwile Leroy and P. J. Cannon, "Skin capillary blood flow in scleroderma," *J. Clin. Invest.* **50**(4), 930–939 (1971).
4. A. K. Murray et al., "Preliminary clinical evaluation of semi-automated nailfold capillaroscopy in the assessment of patients with Raynaud's phenomenon," *Microcirculation* **18**(6), 440–447 (2011).
5. D. Rossi et al., "The role of nail-videocapillaroscopy in early diagnosis of scleroderma," *Autoimmun. Rev.* **12**(8), 821–825 (2013).

6. J. Aellen et al., "Preserved capillary density of dorsal finger skin in treated hypertensive patients with or without type 2 diabetes," *Microcirculation* **19**(6), 554–562 (2012).
7. B. I. Levy et al., "Impaired tissue perfusion—a pathology common to hypertension, obesity, and diabetes mellitus," *Circulation* **118**(9), 968–976 (2008).
8. P. Vajkoczy, A. Ullrich, and M. D. Menger, "Intravital fluorescence videomicroscopy to study tumor angiogenesis and microcirculation," *Neoplasia* **2**(1–2), 53–61 (2000).
9. S. Fantini, "Dynamic model for the tissue concentration and oxygen saturation of hemoglobin in relation to blood volume, flow velocity, and oxygen consumption: implications for functional neuroimaging and coherent hemodynamics spectroscopy (CHS)," *NeuroImage* **85**(1), 202–221 (2014).
10. Y. Yonekura et al., "SPECT with [99mTc]-d,l-hexamethyl-propylene amine oxime (HM-PAO) compared with regional cerebral blood flow measured by PET: effects of linearization," *J. Cereb. Blood Flow Metabol.* **8**(6), S82–S89 (1988).
11. D. J. Heeger and D. Ress, "What does fMRI tell us about neuronal activity?," *Nat. Rev. Neurosci.* **3**(2), 142–151 (2002).
12. J. M. Tarkin, F. R. Joshi, and J. H. F. Rudd, "PET imaging of inflammation in atherosclerosis," *Nat. Rev. Cardiol.* **11**(8), 443–457 (2014).
13. L. W. Dobrucki and A. J. Sinusas, "PET and SPECT in cardiovascular molecular imaging," *Nat. Rev. Cardiol.* **7**(1), 38–47 (2010).
14. J. P. Culver et al., "Diffuse optical tomography of cerebral blood flow, oxygenation, and metabolism in rat during focal ischemia," *J. Cereb. Blood Flow Metab.* **23**(8), 911–924 (2003).
15. A. G. Schneider et al., "Renal perfusion evaluation with contrast-enhanced ultrasonography," *Nephrol. Dial. Transplant.* **27**(2), 674–681 (2012).
16. K. Kalantarinia et al., "Real-time measurement of renal blood flow in healthy subjects using contrast-enhanced ultrasound," *Am. J. Physiol. Renal Physiol.* **297**(4), F1129–F1134 (2009).
17. A. G. Schneider et al., "Contrast-enhanced ultrasound evaluation of the renal microcirculation response to terlipressin in hepato-renal syndrome: a preliminary report," *Ren. Fail.* **37**(1), 175–179 (2015).
18. Z. A. Awan, T. Wester, and K. Kvernebo, "Human microvascular imaging: a review of skin and tongue videomicroscopy techniques and analysing variables," *Clin. Physiol. Funct. Imaging* **30**(2), 79–88 (2010).
19. L. A. Holowatz, C. S. Thompson-Torgerson, and W. L. Kenney, "Last word on viewpoint: the human cutaneous circulation as a model of generalized microvascular function," *J. Appl. Physiol.* **105**(1), 389 (2008).
20. M. Roustit and J. L. Cracowski, "Non-invasive assessment of skin microvascular function in humans: an insight into methods," *Microcirculation* **19**(1), 47–64 (2012).
21. F. Jung et al., "Primary and secondary microcirculatory disorders in essential-hypertension," *Clin. Invest.* **71**(2), 132–138 (1993).
22. P. Coulon, J. Constans, and P. Gosse, "Impairment of skin blood flow during post-occlusive reactive hyperhemy assessed by laser Doppler flowmetry correlates with renal resistive index," *J. Hum. Hypertens.* **26**(1), 56–63 (2012).
23. M. Bukhari et al., "Increased nailfold capillary dimensions in primary Raynaud's phenomenon and systemic sclerosis," *Br. J. Rheumatol.* **35**(11), 1127–1131 (1996).
24. A. L. Herrick, "The pathogenesis, diagnosis and treatment of Raynaud phenomenon," *Nat. Rev. Rheumatol.* **8**(8), 469–479 (2012).
25. P. Kvandal et al., "Regulation of human cutaneous circulation evaluated by laser Doppler flowmetry, iontophoresis, and spectral analysis: importance of nitric oxide and prostaglandines," *Microvasc. Res.* **65**(3), 160–171 (2003).
26. M. Attas et al., "Visualization of cutaneous hemoglobin oxygenation and skin hydration using near-infrared spectroscopic imaging," *Skin Res. Technol.* **7**(4), 238–245 (2001).
27. J. M. Murkin and M. Arango, "Near-infrared spectroscopy as an index of brain and tissue oxygenation," *Br. J. Anaesth.* **103**(Suppl. 1), i3–i13 (2009).
28. I. Seo, P. R. Bargo, and N. Kollias, "Simultaneous assessment of pulsating and total blood in inflammatory skin lesions using functional diffuse reflectance spectroscopy in the visible range," *J. Biomed. Opt.* **15**(6), 060507 (2010).
29. B. Schwarz et al., "Effects of norepinephrine and phenylephrine on intestinal oxygen supply and mucosal tissue oxygen tension," *Intensive Care Med.* **27**(3), 593–601 (2001).
30. M. Hahn et al., "Hemodynamics in nailfold capillaries of patients with systemic scleroderma: synchronous measurements of capillary blood pressure and red blood cell velocity," *J. Invest. Dermatol.* **110**(6), 982–985 (1998).
31. C. C. Wu et al., "Red blood cell velocity measurements of complete capillary in finger nail-fold using optical flow estimation," *Microvasc. Res.* **78**(3), 319–324 (2009).
32. A. Bauer et al., "Monitoring of the sublingual microcirculation in cardiac surgery using orthogonal polarization spectral imaging," *Anesthesiology* **107**(6), 939–945 (2007).
33. O. Genzel-Boroviczeny et al., "Orthogonal polarization spectral Imaging (OPS): a novel method to measure the microcirculation in term and preterm infants transcutaneously," *Pediatr. Res.* **51**(3), 386–391 (2002).
34. C. M. Treu et al., "Sidestream dark weld imaging: the evolution of real-time visualization of cutaneous microcirculation and its potential application in dermatology," *Arch. Dermatol. Res.* **303**(2), 69–78 (2011).
35. W. J. Choi, H. Q. Wang, and R. K. Wang, "Optical coherence tomography microangiography for monitoring the response of vascular perfusion to external pressure on human skin tissue," *J. Biomed. Opt.* **19**(5), 056003 (2014).
36. U. Baran, L. Shi, and R. K. K. Wang, "Capillary blood flow imaging within human finger cuticle using optical microangiography," *J. Biophotonics* **8**(1–2), 46–51 (2015).
37. S. Hu, K. Maslov, and L. V. Wang, "Second-generation optical-resolution photoacoustic microscopy with improved sensitivity and speed," *Opt. Lett.* **36**(7), 1134–1136 (2011).
38. S. Hu et al., "Functional transcranial brain imaging by optical-resolution photoacoustic microscopy," *J. Biomed. Opt.* **14**(4), 040503 (2009).
39. J. J. Yao et al., "In vivo photoacoustic imaging of transverse blood flow by using Doppler broadening of bandwidth," *Opt. Lett.* **35**(9), 1419–1421 (2010).
40. R. Ma et al., "Fast scanning coaxial optoacoustic microscopy," *Biomed. Opt. Express* **3**(7), 1724–1731 (2012).
41. X. L. Deán-Ben and D. Razansky, "Functional optoacoustic human angiography with handheld video rate three dimensional scanner," *Photoacoustics* **1**(3–4), 68–73 (2013).
42. A. P. Jathoul et al., "Deep in vivo photoacoustic imaging of mammalian tissues using a tyrosinase-based genetic reporter," *Nat. Photon.* **9**, 239–246 (2015).
43. P. F. Hai et al., "Near-infrared optical-resolution photoacoustic microscopy," *Opt. Lett.* **39**(17), 5192–5195 (2014).
44. Y. Zhou et al., "Microcirculatory changes identified by photoacoustic microscopy in patients with complex regional pain syndrome type I after stellate ganglion blocks," *J. Biomed. Opt.* **19**(8), 086017 (2014).
45. L. D. Wang et al., "Fast voice-coil scanning optical-resolution photoacoustic microscopy," *Opt. Lett.* **36**(2), 139–141 (2011).
46. C. Yeh et al., "Three-dimensional arbitrary trajectory scanning photoacoustic microscopy," *J. Biophotonics* **8**(4), 303–308 (2015).
47. J. J. Yao et al., "High-speed label-free functional photoacoustic microscopy of mouse brain in action," *Nat. Methods* **12**(5), 407–410 (2015).
48. J. J. Yao et al., "Label-free oxygen-metabolic photoacoustic microscopy in vivo," *J. Biomed. Opt.* **16**(7), 076003 (2011).
49. L. D. Wang, K. Maslov, and L. V. Wang, "Single-cell label-free photoacoustic flowoxigraphy in vivo," *Proc. Natl. Acad. Sci. U. S. A.* **110**(15), 5759–5764 (2013).
50. H. F. Zhang, K. Maslov, and M. Sivaramakrishnan, "Imaging of hemoglobin oxygen saturation variations in single vessels in vivo using photoacoustic microscopy," *Appl. Phys. Lett.* **90**(5), 053901 (2007)
51. X. Wang et al., "Noninvasive imaging of hemoglobin concentration and oxygenation in the rat brain using high-resolution photoacoustic tomography," *J. Biomed. Opt.* **11**(2), 024015 (2006).
52. S. Hu and L. H. V. Wang, "Optical-resolution photoacoustic microscopy: auscultation of biological systems at the cellular level," *Biophys. J.* **105**(4), 841–847 (2013).
53. Y. H. Liao et al., "Quantitative analysis of intrinsic skin aging in dermal papillae by in vivo harmonic generation microscopy," *Biomed. Opt. Express* **5**(9), 3266–3279 (2014).
54. R. O'Rahilly and F. Muller, *Basic Human Anatomy: A Regional Study of Human Structure*, W. B. Saunders Co. (1982).

55. W. Dzwinel, K. Boryczko, and D. A. Yuen, "A discrete-particle model of blood dynamics in capillary vessels," *J. Colloid Interface Sci.* **258**(1), 163–173 (2003).
56. K. Sriram, M. Intaglietta, and D. M. Tartakovsky, "Non-Newtonian flow of blood in arterioles: consequences for wall shear stress measurements," *Microcirculation* **21**(7), 628–639 (2014).
57. H. E. A. Baieth, "Physical parameters of blood as a non-Newtonian fluid," *Int. J. Biomed. Sci.* **4**(4), 323–329 (2008).
58. Y. Zheng et al., "A model of the hemodynamic response and oxygen delivery to brain," *NeuroImage* **16**(3), 617–637 (2002).

Hsun-Chia Hsu is currently a graduate student in biomedical engineering at Washington University in St. Louis under the supervision of Dr. Lihong Wang. He received his BS and MS degrees in physics from National Taiwan University. His research focuses on the development and application of optical-resolution photoacoustic microscopy.

Lidai Wang is an assistant professor in department of mechanical and biomedical engineering at City University of Hong Kong since 2015. He worked as a postdoctoral research fellow in Washington University in St. Louis. His research focuses on biophotonics, biomedical imaging, wavefront engineering, instrumentation, and their biomedical applications. He has published 30 articles in peer-reviewed journals and has received four best paper awards from international conferences.

Lihong V. Wang, the Beare Distinguished Professor at Washington University in St. Louis, has published 450 journal articles (h-index = 104, citations > 43,000) and delivered 440 keynote/plenary/invited talks. His laboratory published the first functional photoacoustic CT and 3D photoacoustic microscopy. He received the Goodman Award for his *Biomedical Optics* textbook, NIH Director's Pioneer Award, OSA Mees Medal, IEEE Technical Achievement and Biomedical Engineering Awards, SPIE Britton Chance Biomedical Optics Award, and an honorary doctorate from Lund University, Sweden.